11th International Symposium on Turbulence and Shear Flow Phenomena (TSFP11)
Southampton, UK, July 30 to August 2, 2019

EFFECT OF FAST ROTATION ON PRESSURE FLUCTUATIONS AND TAYLOR–GÖRTLER-LIKE VORTICES IN CHANNEL FLOWS

Zixuan Yang
State Key Laboratory of Nonlinear Mechanics
Institute of Mechanics, Chinese Academy of Science
Beijing 100190, China
yangzx@imech.ac.cn

Bing-Qing Deng
St. Anthony Falls Laboratory
University of Minnesota
Minneapolis 55414, USA
bdeng@umn.edu

Bing-Chen Wang
Department of Mechanical Engineering
University of Manitoba
Winnipeg R3T 5V6, Canada
bingchen.wang@umanitoba.ca

ABSTRACT

In this paper, the pressure field is decomposed into rotation-induced and convection-induced components to analyze the effects of streamwise system rotation on the pressure fluctuations and the transport of Reynolds stresses. We show analytically that the system rotation acts as a "linear amplifier", which converts high-wavenumber low-amplitude streamwise vorticity fluctuations into low-wavenumber high-amplitude pressure fluctuations, and facilitates the growth of streamwise-elongated Taylor–Görtler-like (TGL) vortices. A new set of transport equations in the spectral space is derived to study the budget balance of velocity-spectrum tensor at different wavelengths. The mechanisms underlying the generation of TGL vortices are explained through the analyses of the budget balance of Reynolds stresses and energy spectra.

Introduction

Turbulent flow in a channel rotating in the streamwise direction is physically complex due to the coexistence of a double S-shaped triple-zero-crossing mean spanwise velocity field (Weller & Oberlack, 2006; Oberlack *et al.*, 2006; Wu & Kasagi, 2004) and two-layers of streamwise-elongated counter-rotating TGL vortices (Yang & Wang, 2018). In their direct numerical simulation (DNS) study of streamwise-rotating channel flow at a very high rotation number (up to $Ro_\tau = 2\Omega h/u_\tau = 150$, where Ω, h, and u_τ represent the angular speed of the system rotation, one-half the channel height, and the mean friction velocity, repsectively), Yang & Wang (2018) reported that the TGL vortices play an important role in momentum transfer and influence significantly the flow statistics. They also studied the transport equations of Reynolds stresses, and observed that the pressure term increases rapidly in magnitude with an increasing rotation number and plays an important role in the budget balance of Reynolds stresses at a very high rotation number. However, it is not clear why the pressure term is sensitive to the system rotation, and how the system rotation transfers turbulence kinetic energy between different Reynolds stress components to sustain the TGL vortices.

In this research, we aim at finding answers to the above important questions. Through an analysis of the transport equations of Reynolds stresses in both physical and spectral spaces, we demonstrate the modulating effects of system rotation on pressure fluctuations, which significantly influences the size, strength and characteristic wavelength of TGL vortices in a fast streamwise-rotating flow.

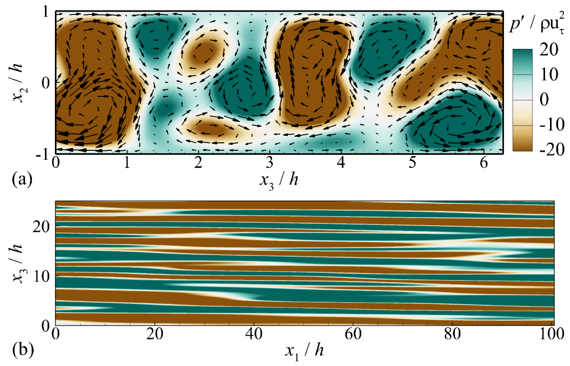

Figure 1. TGL vortices visualized using the contours of pressure fluctuation p' at $Ro_\tau = 150$ in (a) x_2–x_3 plane at $x_1 = 0$ and (b) x_1–x_3 plane at $x_2/h = -0.5$. Vectors consisting of u'_2 and u'_3 are superimposed in panel (a) to show the rotating direction of the vortices.

Numerical Method and Test Cases

The DNS was conducted using an in-house pseudo-spectral method code (Yang & Wang, 2018). The new findings are obtained by analyzing the DNS database with the rotation number varying from 0 to 150. The highest rotation number ($Ro_\tau = 150$) analyzed here is the highest for streamwise-rotating flows in the literature. A very long computational domain of $L_1 \times L_2 \times L_3 = 512\pi h \times 2h \times 8\pi h$ (with $16384 \times 128 \times 256$ grid points) has been used to perform DNS at $Ro_\tau = 150$ to capture the streamwise-elongated vortex structures. In order to focus our study on the effect of rotation number on the TGL vortices, the Reynolds number is fixed to $Re_\tau = u_\tau h/\nu = 180$ in all cases, where ν is the kinematic viscosity of the fluid. In presenting the results, we use a pair of angular brackets $\langle\cdot\rangle$ to denote temporal- and plane-averaging, and subsequently, the fluctuating component of an arbitrary variable ϕ is determined as $\phi' = \phi - \langle\phi\rangle$.

Decomposition of Pressure Fluctuations

Figure 1 shows typical vortex structures at $Ro_\tau = 150$ in both cross-stream (x_2–x_3) and horizontal (x_1–x_3) planes. From Fig. 1(a), it is observed that positive and negative pressure fluctuations p' collocate with the large-scale vortices rotating in the counter-clockwise and clockwise directions, respectively. Figure 1(b) shows that the TGL vortices visualized using the contours of instantaneous pressure fluc-

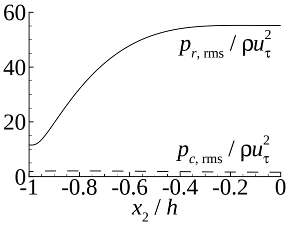

Figure 2. Profiles of $p_{r,\mathrm{rms}}$ and $p_{c,\mathrm{rms}}$ at $Ro_\tau = 150$.

tuations p' are elongated in the streamwise direction.

To further study the effect of system rotation on the pressure field, we take the divergence of momentum equation and apply the divergence-free condition to obtain the following Poisson equation for pressure, viz.

$$\frac{1}{\rho}\frac{\partial^2 p}{\partial x_i \partial x_i} = -\frac{\partial u_i}{\partial x_j}\frac{\partial u_j}{\partial x_i} + 2\Omega\omega_1 \quad , \tag{1}$$

where $\omega_1 \stackrel{\text{def}}{=} \partial u_3/\partial x_2 - \partial u_2/\partial x_3$ is the streamwise vorticity. The boundary condition of the pressure field reads

$$\frac{\partial p}{\partial x_2} = \rho\nu\frac{\partial^2 u_2}{\partial x_2^2} \quad \text{at} \quad x_2 = \pm h \quad . \tag{2}$$

The pressure can be further decomposed into a rotation-induced component p_r and a convection-induced component p_c, governed by the following two Poisson equations, respectively:

$$\begin{cases} \dfrac{1}{\rho}\dfrac{\partial^2 p_r}{\partial x_i \partial x_i} = 2\Omega\omega_1 \quad , \\ \dfrac{1}{\rho}\dfrac{\partial^2 p_c}{\partial x_i \partial x_i} = -\dfrac{\partial u_i}{\partial x_j}\dfrac{\partial u_j}{\partial x_i} \quad . \end{cases} \tag{3}$$

Correspondingly, the boundary condition (2) can be decomposed into

$$\left.\begin{aligned} \frac{\partial p_r}{\partial x_2} &= 0 \\ \frac{\partial p_c}{\partial x_2} &= \rho\nu\frac{\partial^2 u_2}{\partial x_2^2} \end{aligned}\right\} \quad \text{at} \quad x_2 = \pm h \quad . \tag{4}$$

Because Eqs. (3)–(4) are linear with respect to the pressure, $p \equiv p_r + p_c$ holds strictly.

Figure 2 compares the profiles of the root-mean-square (RMS) of pressure fluctuations $p_{r,\mathrm{rms}}$ and $p_{c,\mathrm{rms}}$ at $Ro_\tau = 150$. As shown in the figure, the magnitude of $p_{r,\mathrm{rms}}$ is significantly larger than that of $p_{c,\mathrm{rms}}$ at $Ro_\tau = 150$, indicating the dominance of rotation-induced over convection-induced pressure fluctuations. In order to understand this dominant effect of $p_{r,\mathrm{rms}}$, Figs. 3(a) and 3(b) compare the profiles of $\omega_{1,\mathrm{rms}}$ and $p_{r,\mathrm{rms}}$ at various rotation numbers, respectively. As shown in Fig. 3(a), in general, the magnitude of $\omega_{1,\mathrm{rms}}$ is insensitive to Ro_τ. From Eq. (3), it is clear that the role of system rotation (as indicated by Ω) is to linearly amplify the conversion of the streamwise vorticity fluctuations ω_1' into the rotation-induced pressure fluctuations p_r'. Because the magnitude of ω_1' is insensitive to Ro_τ, the value of $p_{r,\mathrm{rms}}$ grows almost linearly with respect to Ro_τ.

Effect of System Rotation on Budget Balance of Reynolds Stresses

In order to study the effect of strong pressure fluctuations on the Reynolds stresses, we consider the following transport equation of Reynolds stresses

$$\frac{\partial E_{ij}}{\partial t} = 0 = P_{ij} + C_{ij} + \Pi_{ij}^r + \Pi_{ij}^c + \varepsilon_{ij} + T_{ij} + D_{ij} \quad . \tag{5}$$

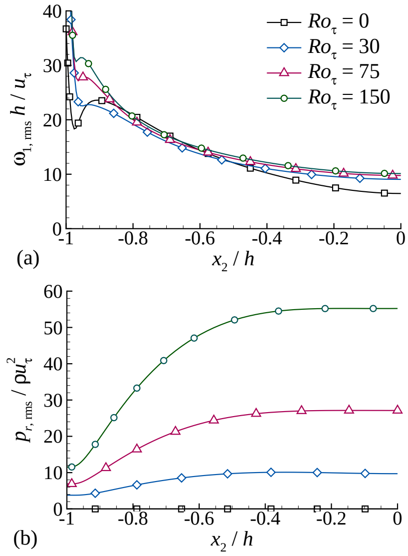

Figure 3. Profiles of (a) $\omega_{1,\mathrm{rms}}$ and (b) $p_{r,\mathrm{rms}}$ at various rotation numbers.

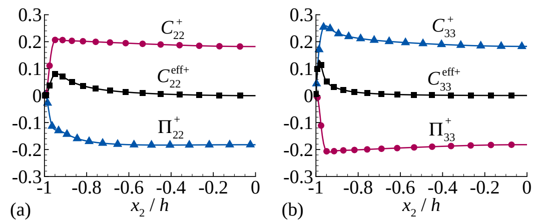

Figure 4. Profiles of the Coriolis term C_{ij}^+, rotation-induced pressure term Π_{ij}^{r+} and effective rotation term $C_{ij}^{\mathrm{eff}+}$ in the transport equation of (a) $\langle u_2'u_2'\rangle^+$ and (b) $\langle u_3'u_3'\rangle^+$ at $Ro_\tau = 150$.

Here, P_{ij}, C_{ij}, Π_{ij}^r, Π_{ij}^c, ε_{ij}, T_{ij}, and D_{ij} denote the production term, Coriolis term, rotation-induced pressure term, convection-induced pressure term, viscous dissipation term, turbulent diffusion term, and viscous diffusion term, respectively, which are defined as

$$\begin{aligned}
P_{ij} &= -\left(\langle u_i'u_k'\rangle\frac{\partial\langle u_j\rangle}{\partial x_k} + \langle u_j'u_k'\rangle\frac{\partial\langle u_i\rangle}{\partial x_k}\right) \quad , && (6)\\
C_{ij} &= 2\Omega(\varepsilon_{1ik}\langle u_j'u_k'\rangle + \varepsilon_{1jk}\langle u_i'u_k'\rangle) \quad , && (7)\\
\Pi_{ij}^r &= -\frac{1}{\rho}\left\langle u_i'\frac{\partial p_r'}{\partial x_j} + u_j'\frac{\partial p_r'}{\partial x_i}\right\rangle \quad , && (8)\\
\Pi_{ij}^c &= -\frac{1}{\rho}\left\langle u_i'\frac{\partial p_c'}{\partial x_j} + u_j'\frac{\partial p_c'}{\partial x_i}\right\rangle \quad , && (9)\\
\varepsilon_{ij} &= -2\nu\left\langle\frac{\partial u_i'}{\partial x_k}\frac{\partial u_j'}{\partial x_k}\right\rangle \quad , && (10)\\
T_{ij} &= -\frac{\partial\langle u_i'u_j'u_k'\rangle}{\partial x_k} \quad , && (11)\\
D_{ij} &= \nu\frac{\partial^2\langle u_i'u_j'\rangle}{\partial x_k\partial x_k} \quad . && (12)
\end{aligned}$$

Both the Coriolis term C_{ij} and the rotation-induced pressure term Π_{ij}^r are direct consequences of system rotation. In order to evaluate the general effect of system rotation on the transport equation of Reynolds stresses, it is useful to further define an effective (or, total) rotation term $C_{ij}^{\mathrm{eff}} \stackrel{\text{def}}{=} C_{ij} + \Pi_{ij}^r$. To demonstrate the necessity of introducing the concept of C_{ij}^{eff} in the analysis, Fig. 4 compares the profiles of the effective rotation term $C_{ij}^{\mathrm{eff}+}$, Coriolis ter-

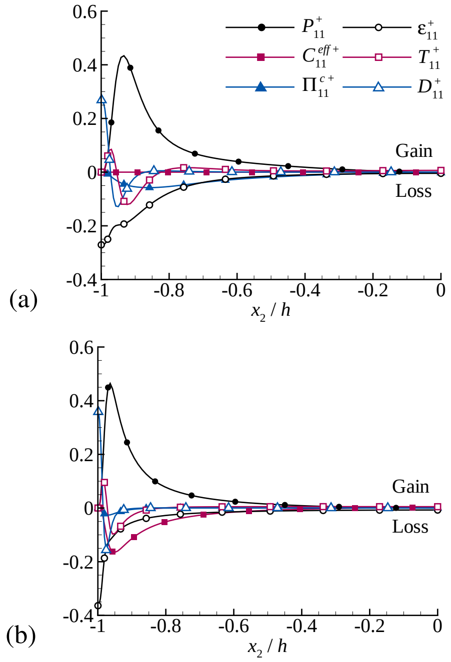

Figure 5. Profiles of budget terms in the transport equation of Reynolds normal stress $\langle u_1' u_1' \rangle^+$ in (a) non-rotating ($Ro_\tau = 0$) and (b) streamwise-rotating ($Ro_\tau = 150$) turbulent channel flows.

m C_{ij}^+ and rotation-induced pressure term Π_{ij}^{r+} for $\langle u_2' u_2' \rangle^+$ and $\langle u_3' u_3' \rangle^+$ at $Ro_\tau = 150$. Here, superscript "+" denotes physical quantities non-dimensionalized using u_τ and ν / u_τ as the characteristic velocity and length scales, respectively. As shown in the figures, the net rotation effect as represented by the effective rotation term $C_{ij}^{\mathrm{eff}+}$ is much smaller than either C_{ij}^+ or Π_{ij}^{r+}. The effect of the system rotation on the transport of Reynolds stresses would be misidentified if only the Coriolis term C_{ij}^+ was considered. For example, if the attention is solely paid to the Coriolis term C_{33}^+, it would lead to a wrong conclusion that $\langle u_3' u_3' \rangle^+$ loses energy due to the effect of rotation. In fact, the effective rotation term $C_{33}^{\mathrm{eff}+}$ is positive, indicating the net effect of streamwise system rotation is to 'power' $\langle u_3' u_3' \rangle^+$.

Figures 5–7 compare the budget terms in the transport equations of Reynolds normal stresses of the non-rotating ($Ro_\tau = 0$) and streamwise-rotating ($Ro_\tau = 150$) turbulent channel flows. As is evident in Figs. 5(a), 6(a) and 7(a), in the non-rotating channel flow, the dissipation terms ε_{11}^+, ε_{22}^+ and ε_{33}^+ are the dominant sinks in the transport equations of $\langle u_1' u_1' \rangle^+$, $\langle u_2' u_2' \rangle^+$ and $\langle u_3' u_3' \rangle^+$, respectively. The function of these dissipation terms is to balance either the production term P_{11}^+ or convection-induced pressure terms Π_{22}^{c+} and Π_{33}^{c+} in a non-rotating channel flow, an observation that is consistent with the result of Mansour *et al.* (1988).

The budget balance of Reynolds normal stresses in a fast rotating channel flow is fundamentally different from that in a non-rotating channel flow. As shown in figure 5(b), in comparison with the non-rotating case ($Ro_\tau = 0$), although the magnitude of ε_{11}^+ is slightly larger at the wall in the fast rotating case ($Ro_\tau = 150$), it drops more rapidly as the wall-normal distance increases beyond $x_2/h = -0.97$. Furthermore, the effective rotation term $C_{11}^{\mathrm{eff}+}$ becomes the dominant sink in a considerably large region ($-0.97 < x_2/h < -0.55$) at $Ro_\tau = 150$. The energy drained from $\langle u_1' u_1' \rangle^+$ by $C_{11}^{\mathrm{eff}+}$ is fed to $\langle u_2' u_2' \rangle^+$ and $\langle u_3' u_3' \rangle^+$. As

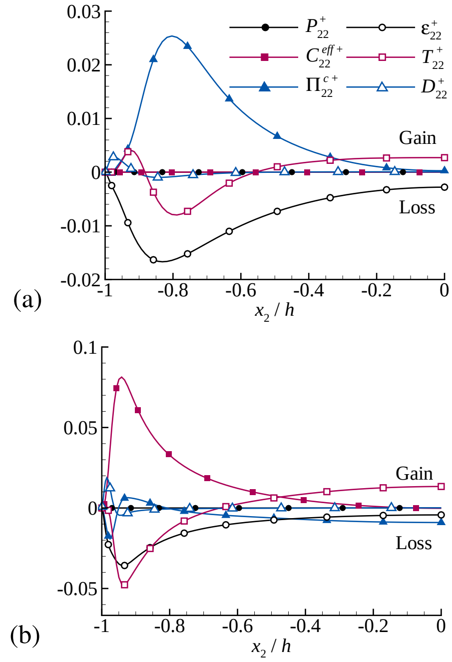

Figure 6. Profiles of budget terms in the transport equation of Reynolds normal stress $\langle u_2' u_2' \rangle^+$ in (a) non-rotating ($Ro_\tau = 0$) and (b) streamwise-rotating ($Ro_\tau = 150$) turbulent channel flows.

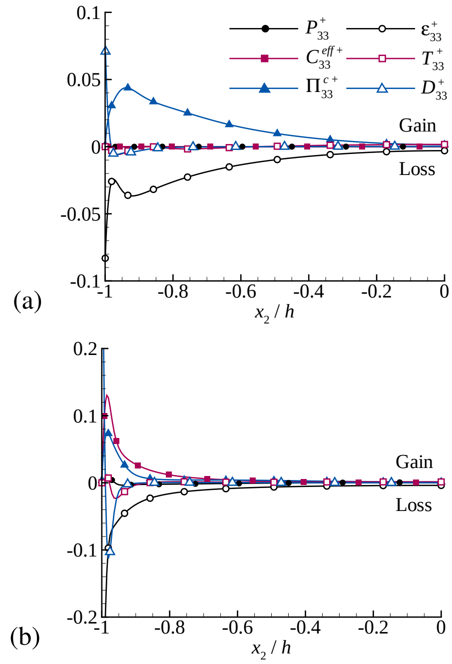

Figure 7. Profiles of budget terms in the transport equation of Reynolds normal stress $\langle u_3' u_3' \rangle^+$ in (a) non-rotating ($Ro_\tau = 0$) and (b) streamwise-rotating ($Ro_\tau = 150$) turbulent channel flows.

shown in figures 6(b) and 7(b), the effective rotation terms $C_{22}^{\mathrm{eff}+}$ and $C_{33}^{\mathrm{eff}+}$ are both positively valued, acting as sources for $\langle u_2' u_2' \rangle^+$ and $\langle u_3' u_3' \rangle^+$, respectively. In consequence, in comparison with the non-rotating case, the magnitudes of viscous dissipation rates ε_{22}^+ and ε_{33}^+ are amplified in the same region to balance the additional TKE transported from the streamwise to the spanwise and wall-normal velocity fluctuations in a fast streamwise-rotating channel flow.

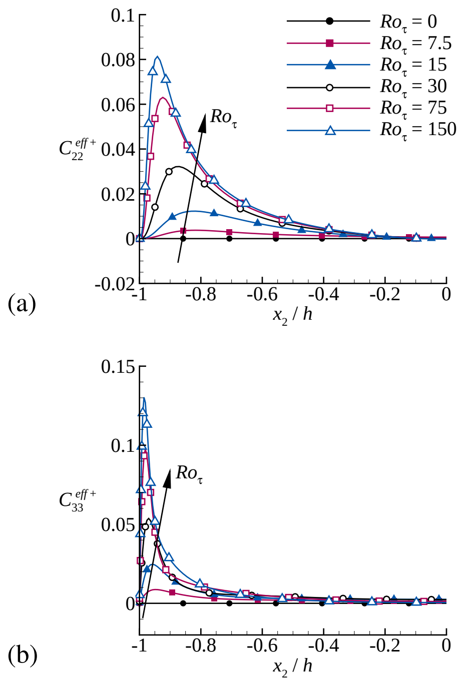

Figure 8. Profiles of the effective rotation terms (a) $C_{22}^{\mathrm{eff}+}$ and (b) $C_{33}^{\mathrm{eff}+}$ at various rotation numbers. The arrow points to the direction of an increasing rotation number.

To deepen the study of the rotating effects on the magnitude of the effective rotation term, Fig. 8 compares the profiles of $C_{22}^{\mathrm{eff}+}$ and $C_{33}^{\mathrm{eff}+}$ at various rotation numbers. As shown in the figure, the magnitudes of both $C_{22}^{\mathrm{eff}+}$ and $C_{33}^{\mathrm{eff}+}$ increase monotonically as the rotation number increases, indicating that the system rotation tends to enhance the wall-normal and spanwise velocity fluctuations, further promoting the formation and motion of large-scale TGL vortices in a cross-stream (x_2–x_3) plane. This explains the previous observation that TGL vortices become more active and streamwise elongated as the rotation number increases (Yang & Wang, 2018).

Effect of System Rotation on Budget Balance of Energy Spectra

The transport of Reynolds stresses can be studied precisely in not only the physical space but also the spectral space. One of the major objectives of this research is on the elucidation of the mechanisms underlying the streamwise-elongated TGL vortices observed in Yang & Wang (2018). To this purpose, we define the Fourier transform of an arbitrary variable $\phi(x_1,x_2,x_3,t)$ in the streamwise direction as

$$\hat{\phi}(k_1,x_2,x_3,t) = \frac{1}{L_1}\int_0^{L_1} \phi(x_1,x_2,x_3,t) e^{-\mathrm{i}k_1x_1}\mathrm{d}x_1 \quad , \quad (13)$$

where $\mathrm{i} = \sqrt{-1}$ is the imaginary unit, and $k_1 = n_1 k_{01}$ is the streamwise wavenumber. Here, $n_1 \in [-N_1/2, N_1/2-1]$ is an integer, and $k_{01} = 2\pi/L_1$ is the lowest positive wavenumbers in the streamwise direction. By applying the above Fourier transform to the momentum equation that governs the instantaneous velocity fluctuations and after some derivation, the following transport equation of Reynolds stresses in the spectral space is obtained

$$\frac{\partial \tilde{E}_{ij}}{\partial t} = 0 = \tilde{P}_{ij} + \tilde{C}_{ij}^{\mathrm{eff}} + \tilde{\Pi}_{ij}^{c} + \tilde{\varepsilon}_{ij} + \tilde{D}_{ij} + \tilde{T}_{ij} \quad . \quad (14)$$

Here, $\tilde{E}_{ij} = \mathrm{Re}\{\hat{R}_{ij}(k_1,x_2)\} = \mathrm{Re}\{\overline{\widehat{u'_i}^* \widehat{u'_j}}\}$ is the co-spectrum between u'_i and u'_j, where $\hat{R}_{ij}$ is the Fourier coefficient of the two-point velocity correlation function $R_{ij}(r_1,x_2) = \langle u'_i(x_1,x_2,x_3,t)u'_j(x_1+r_1,x_2,x_3,t)\rangle$, superscript * and $\mathrm{Re}\{\}$ denote the conjugate and real part of a complex number, respectively. The overline represents time and spanwise averaging. The budget terms on the right hand side (RHS) of Eq. (14) are defined as

$$\tilde{P}_{ij} = \mathrm{Re}\left\{-\overline{\widehat{u'_j}\widehat{u'_2}^*}\frac{\partial\langle u_i\rangle}{\partial x_2} - \overline{\widehat{u'_i}^*\widehat{u'_2}}\frac{\partial\langle u_j\rangle}{\partial x_2}\right\} \quad , \quad (15)$$

$$\begin{aligned}\tilde{C}_{ij}^{\mathrm{eff}} = \mathrm{Re}\Bigg\{ & -2\Omega\left(\varepsilon_{i1k}\overline{\widehat{u'_j}\widehat{u'_k}^*} + \varepsilon_{j1k}\overline{\widehat{u'_i}^*\widehat{u'_k}}\right) \\ & -\frac{1}{\rho}\mathrm{i}k_1\left(\overline{\widehat{p'_r}^*\widehat{u'_j}}\delta_{i1} - \overline{\widehat{p'_r}\widehat{u'_i}^*}\delta_{j1}\right) \\ & -\frac{1}{\rho}\left(\overline{\frac{\partial\widehat{p'_r}^*}{\partial x_2}\widehat{u'_j}}\delta_{i2} + \overline{\frac{\partial\widehat{p'_r}}{\partial x_2}\widehat{u'_i}^*}\delta_{j2}\right) \\ & -\frac{1}{\rho}\left(\overline{\frac{\partial\widehat{p'_r}^*}{\partial x_3}\widehat{u'_j}}\delta_{i3} + \overline{\frac{\partial\widehat{p'_r}}{\partial x_3}\widehat{u'_i}^*}\delta_{j3}\right)\Bigg\} \quad , \quad (16)\end{aligned}$$

$$\begin{aligned}\tilde{\Pi}_{ij}^{c} = \mathrm{Re}\Bigg\{ & -\frac{1}{\rho}\mathrm{i}k_1\left(\overline{\widehat{p'_c}^*\widehat{u'_j}}\delta_{i1} - \overline{\widehat{p'_c}\widehat{u'_i}^*}\delta_{j1}\right) \\ & -\frac{1}{\rho}\left(\overline{\frac{\partial\widehat{p'_c}^*}{\partial x_2}\widehat{u'_j}}\delta_{i2} + \overline{\frac{\partial\widehat{p'_c}}{\partial x_2}\widehat{u'_i}^*}\delta_{j2}\right) \\ & -\frac{1}{\rho}\left(\overline{\frac{\partial\widehat{p'_c}^*}{\partial x_3}\widehat{u'_j}}\delta_{i3} + \overline{\frac{\partial\widehat{p'_c}}{\partial x_3}\widehat{u'_i}^*}\delta_{j3}\right)\Bigg\} \quad , \quad (17)\end{aligned}$$

$$\tilde{\varepsilon}_{ij} = \mathrm{Re}\left\{-2\nu\left(k_1^2\overline{\widehat{u'_i}^*\widehat{u'_j}} + \overline{\frac{\partial\widehat{u'_i}^*}{\partial x_2}\frac{\partial\widehat{u'_j}}{\partial x_2}} + \overline{\frac{\partial\widehat{u'_i}^*}{\partial x_3}\frac{\partial\widehat{u'_j}}{\partial x_3}}\right)\right\} \quad , \quad (18)$$

$$\tilde{D}_{ij} = \mathrm{Re}\left\{\nu\frac{\partial^2\overline{\widehat{u'_i}^*\widehat{u'_j}}}{\partial x_2^2}\right\} \quad , \quad (19)$$

$$\begin{aligned}\tilde{T}_{ij} = \mathrm{Re}\Bigg\{ & -\mathrm{i}k_1\left(\overline{\widehat{u'_j}\widehat{u'_iu'_1}^*} - \overline{\widehat{u'_i}^*\widehat{u'_ju'_1}}\right) \\ & -\overline{\frac{\partial\widehat{u'_iu'_2}^*}{\partial x_2}\widehat{u'_j}} - \overline{\frac{\partial\widehat{u'_ju'_2}}{\partial x_2}\widehat{u'_i}^*} \\ & -\overline{\frac{\partial\widehat{u'_iu'_3}^*}{\partial x_3}\widehat{u'_j}} - \overline{\frac{\partial\widehat{u'_ju'_3}}{\partial x_3}\widehat{u'_i}^*}\Bigg\} \quad . \quad (20)\end{aligned}$$

To further study the effect of system rotation on the scales of TGL vortices, the transport equations of energy spectra $\tilde{E}_{11}^+$, $\tilde{E}_{22}^+$ and $\tilde{E}_{33}^+$ (of three Reynolds normal stress components) need to be investigated. Figure 9 compares the pre-multiplied budget terms in the transport equation of $\tilde{E}_{11}^+$ in non-rotating ($Ro_\tau = 0$) and streamwise-rotating ($Ro_\tau = 150$) channel flows at $x_2/h = -0.5$, where the flow field is significantly influenced by TGL vortices. From Fig. 9, it is seen that the streamwise wavelength corresponding to the peak of the pre-multiplied production term $k_1^+\tilde{P}_{11}^+$ is approximately $\lambda_1/h = 200$ at $Ro_\tau = 150$, but is only 2.6 at $Ro_\tau = 0$. This indicates that the TKE is produced at larger wavelengths in a fast streamwise-rotating channel due to the occurrence of large-scale TGL vortices.

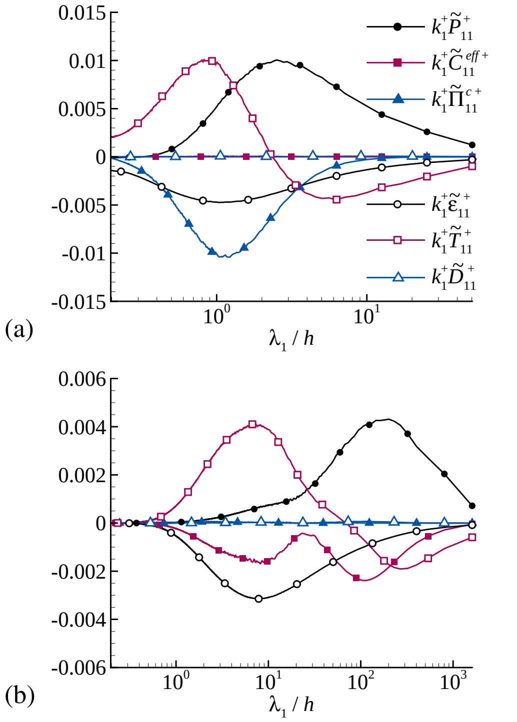

Figure 9. Pre-multiplied budget terms in the transport equation of spectrum $\tilde{E}_{11}^+$ at $x_2/h = -0.5$ for (a) non-rotating ($Ro_\tau = 0$) and (b) streamwise-rotating ($Ro_\tau = 150$) turbulent channel flows.

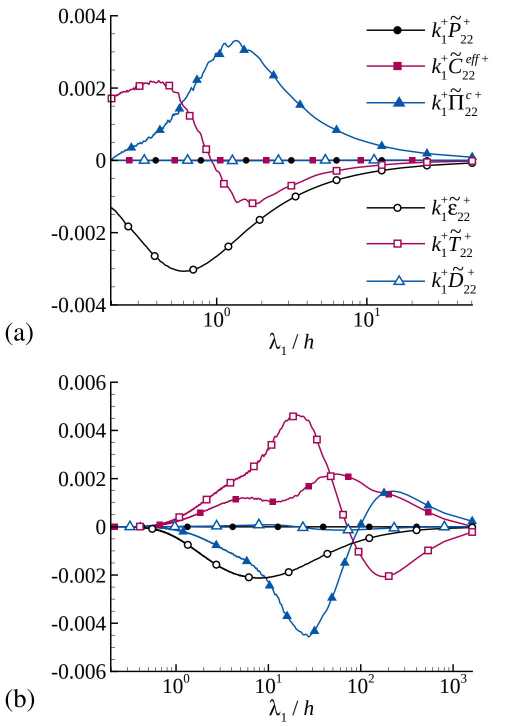

Figure 10. Pre-multiplied budget terms in the transport equation of spectrum $\tilde{E}_{22}^+$ at $x_2/h = -0.5$ for (a) non-rotating ($Ro_\tau = 0$) and (b) streamwise-rotating ($Ro_\tau = 150$) turbulent channel flows.

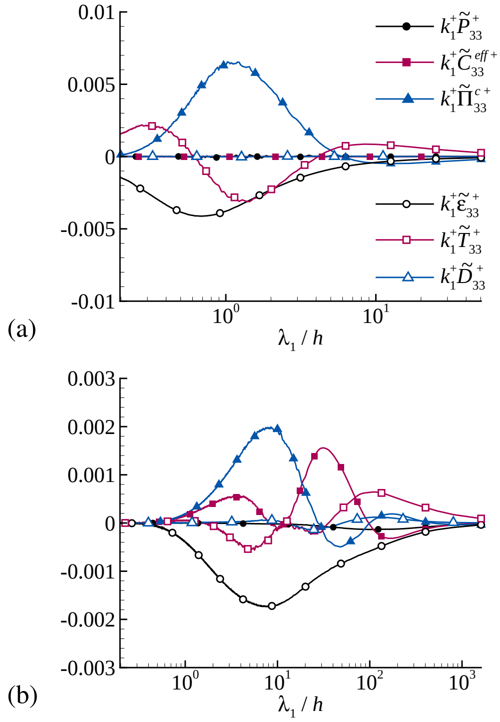

Figure 11. Pre-multiplied budget terms in the transport equation of spectrum $\tilde{E}_{33}^+$ at $x_2/h = -0.5$ for (a) non-rotating ($Ro_\tau = 0$) and (b) streamwise-rotating ($Ro_\tau = 150$) turbulent channel flows.

Figure 9(a) shows that in the non-rotating channel, the convection-induced pressure term $\tilde{\Pi}_{11}^{c+}$ and dissipation term $\tilde{\varepsilon}_{11}^+$ are the two dominant terms consuming the TKE. The characteristic wavelength corresponding to the mode of either $\tilde{\Pi}_{11}^{c+}$ or $\tilde{\varepsilon}_{11}^+$ is $\lambda_1/h = 1.2$ (or equivalently, 216 wall units). In the streamwise-rotating channel, as shown in Fig. 9(b), the dissipation term remains important, but the convection-induced pressure term $\tilde{\Pi}_{11}^{c+}$ becomes negligible. The role of $\tilde{\Pi}_{11}^{c+}$ in a non-rotating channel flow is replaced by the effective rotation term $\tilde{C}_{11}^{\mathrm{eff}+}$ in a streamwise-rotating channel flow, an observation that is consistent with the analysis of the budget balance of $\langle u_1' u_1' \rangle^+$ in the physical space based on Fig. 5. As shown in Fig. 9(b), there are two negatively valued peaks in the profile of $k_1^+\tilde{C}_{11}^{\mathrm{eff}+}$ at $Ro_\tau = 150$. The primary peak occurs at $\lambda_1/h = 100$ (or equivalently, 1.8×10^4 wall units), and the secondary peak occurs at a much smaller wavelength of $\lambda_1/h = 8$ (or equivalently, 1440 wall units). The primary peak of $k_1^+\tilde{C}_{11}^{\mathrm{eff}+}$ corresponds to the streamwise scale of TGL vortices observed by Yang & Wang (2018). The secondary peak of $k_1^+\tilde{C}_{11}^{\mathrm{eff}+}$ collocates with the peaks of the pre-multiplied turbulent diffusion term $k_1^+\tilde{T}_{11}^+$ and viscous dissipation term $k_1^+\tilde{\varepsilon}_{11}^+$. From Figs. 9(a) and 9(b), it is clear that the value of $k_1^+\tilde{T}_{11}^+$ is positive and negative at small and large wavelengths, respectively, indicating the transport of TKE from large to small wavelengths. For the fast streamwise-rotating channel flow case shown in Fig. 9(b), the TKE transferred to the streamwise velocity fluctuations at small wavelength ($\lambda_1/h = 8$) by the turbulent diffusion term $\tilde{T}_{11}^+$ is then partially drained by the viscous dissipation term $\tilde{\varepsilon}_{11}^+$ and partially carried away by the effective rotation term $\tilde{C}_{11}^{\mathrm{eff}+}$ to feed $\tilde{E}_{22}^+$ and $\tilde{E}_{33}^+$ according to the above discussions.

Figures 10 and 11 show the pre-multiplied budget terms in the transport equations of streamwise spectra $\tilde{E}_{22}^+$

and $\tilde{E}_{33}^{+}$, respectively. The results of the non-rotating ($Ro_\tau = 0$) and streamwise-rotating ($Ro_\tau = 150$) channel flows at $x_2/h = -0.5$ are compared. As shown in Figs. 10(a) and 11(a), in the non-rotating channel flow, the convection-induced pressure terms $k_1^+\tilde{\Pi}_{22}^{c+}$ and $k_1^+\tilde{\Pi}_{33}^{c+}$ are dominant sources in the transport equations of $\tilde{E}_{22}^{+}$ and $\tilde{E}_{33}^{+}$, respectively. In contrast, as shown in Fig. 10(b), in the streamwise-rotating channel flow, $k_1^+\tilde{\Pi}_{22}^{c+}$ is positively valued at small wavelengths but becomes negatively valued at large wavelengths. The profile shape of $k_1^+\tilde{\Pi}_{22}^{c+}$ is almost a mirror image of that of $k_1^+\tilde{T}_{22}^{+}$ in Fig. 10(b), indicating that the kinetic energy of the wall-normal velocity fluctuations constructed and destructed by $k_1^+\tilde{T}_{22}^{+}$ at small and large wavelengths, respectively, is directly balanced by $k_1^+\tilde{\Pi}_{22}^{c+}$ (at the same wavelengths). Also from Fig. 10(b), the magnitude of the $k_1^+\tilde{C}_{22}^{\mathrm{eff}+}$ is comparable to that of $k_1^+\tilde{\varepsilon}_{22}^{+}$, with the difference that $k_1^+\tilde{\varepsilon}_{22}^{+}$ is negatively valued and peaks at a smaller wavelength of $\lambda_1/h = 7$ (corresponding to $\lambda_1^+ = 1260$), while $k_1^+\tilde{C}_{22}^{\mathrm{eff}+}$ is positively valued and peaks at a larger wavelength of $\lambda_1/h = 50$ (corresponding to $\lambda_1^+ = 9000$). The physical explanation is that the rotating effect tends to enhance the wall-normal velocity fluctuations at large streamwise wavelengths to form TGL vortex motions. This part of energy constructed by $\tilde{C}_{22}^{\mathrm{eff}+}$ is transported to small wavelengths by the combined effects of $\tilde{\Pi}_{22}^{c+}$ and $\tilde{T}_{22}^{c+}$ through the convection and turbulent diffusion mechanisms, and eventually destructed by $\tilde{\varepsilon}_{22}^{+}$ through the viscous dissipation.

By comparing Fig. 10(b) with Fig. 9(b), it is clear that the values of $k_1^+\tilde{C}_{11}^{\mathrm{eff}+}$ and $k_1^+\tilde{C}_{22}^{\mathrm{eff}+}$ are negative and positive, respectively, at all wavelengths. Furthermore, as shown in Fig. 11(b), although the profile of $k_1^+\tilde{C}_{33}^{\mathrm{eff}+}$ exhibits a complex pattern, its value is mostly positive, especially at small and moderate wavelengths. This observation in the spectral space further confirms the previous conclusion (drawn in the physical space based on the analysis of Figs. 5–7) that the general effect of streamwise system rotation is to extract TKE from the streamwise component $\langle u_1'u_1'\rangle^+$ to the wall-normal and spanwise components $\langle u_2'u_2'\rangle^+$ and $\langle u_3'u_3'\rangle^+$ of Reynolds normal stresses. Figure 11(b) shows that in the transport equation of $\tilde{E}_{33}^{+}$, the convection-induced pressure term $\tilde{\Pi}_{33}^{c+}$ is still an important source at small wavelengths for $\lambda_1/h < 20$ at $Ro_\tau = 150$. At large wavelengths, the spanwise velocity fluctuations gain energy from the effective rotation term $\tilde{C}_{33}^{\mathrm{eff}+}$ and turbulent diffusion term $\tilde{T}_{33}^{+}$. In both non-rotating and rotating channel flows, the destruction of TKE associated with $\langle u_3'u_3'\rangle^+$ is dominated by the dissipation term $\tilde{\varepsilon}_{33}^{+}$ at all wavelengths.

Conclusions

The transport equations of Reynolds stresses are studied in both physical and spectral spaces to investigate the dynamics of TGL vortices. The pressure field is decomposed linearly into a rotation-induced and a convection-induced components (p_r' and p_c', respectively), governed by two independent Poisson equations. The Coriolis force acts on the pressure field as a source term in the Poisson equation that governs the value of p_r'. As the rotation number increases, the magnitude of $p_{r,rms}$ increases linearly, and becomes dominant at a very high rotation number.

In the transport equation of Reynolds stresses, the rotation-induced pressure term Π_{ij}^{r+} is absent in a non-rotating channel flow, however, in a streamwise-rotating channel flow, its influence on the flow field increases rapidly as the rotation number increases. In the budget balances of $\langle u_2'u_2'\rangle^+$ and $\langle u_3'u_3'\rangle^+$, the behaviors of the Coriolis term C_{ij}^{+} and rotation-induced pressure term Π_{ij}^{r+} are opposite of each other, canceling out their net contribution to the transport of Reynolds stresses. As a result, the effect of the system rotation on the transport of Reynolds stresses can be completely misidentified if only the Coriolis term C_{ij}^{+} is considered. As a remedy, an effective rotation term $C_{ij}^{\mathrm{eff}+}$ is defined as the summation of C_{ij}^{+} and Π_{ij}^{r+}. The proposed effective rotation term is able to facilitate a precise diagnose of the general effect of streamwise system rotation on the transport of Reynolds stresses in both physical and spectral analyses.

The effective rotation term is responsible for sustaining TGL vortices in a streamwise-rotating channel flow. From the analyses of transport equations of Reynolds normal stresses, it is discovered that the effective rotation term extracts energy from $\langle u_1'u_1'\rangle^+$ to feed $\langle u_2'u_2'\rangle^+$ and $\langle u_3'u_3'\rangle^+$. The magnitudes of both $C_{22}^{\mathrm{eff}+}$ and $C_{33}^{\mathrm{eff}+}$ increase monotonically as the rotation number increases, indicating that the system rotation tends to enhance the wall-normal and spanwise velocity fluctuations, promoting the formation and motion of large-scale TGL vortices in the cross-stream direction. Further analyses in the spectral space indicate that the energy transfer among three Reynolds normal stresses occurs at large wavelengths. In contrast to a non-rotating channel flow, a significant amount of TKE is produced at large wavelengths by the streamwise velocity fluctuations in a fast streamwise-rotating channel due to the occurrence of large-scale TGL vortices. The TKE produced by TGL vortices is then partially drained by the dissipation term $\tilde{\varepsilon}_{11}^{+}$ and partially carried by the effective rotation term $\tilde{C}_{11}^{\mathrm{eff}+}$ to enhance the wall-normal and spanwise energy spectra $\tilde{E}_{22}^{+}$ and $\tilde{E}_{33}^{+}$. The characteristic wavelengths corresponding to the modes of pre-multiplied effective rotation terms $k_1^+\tilde{C}_{22}^{\mathrm{eff}+}$ and $k_1^+\tilde{C}_{33}^{\mathrm{eff}+}$ increase monotonically with an increasing rotation number, further indicating that the streamwise system rotation tends to elongate the TGL vortices in the streamwise direction.

REFERENCES

Mansour, N. N., Kim, J. & Moin, P. 1988 Reynolds-stress and dissipation-rate budgets in a turbulent channel flow. *J. Fluid Mech.* **194**, 15–44.

Oberlack, M., Cabot, W., Reif, B. A. P. & Weller, T. 2006 Group analysis, direct numerical simulation and modelling of a turbulent channel flow with streamwise rotation. *J. Fluid Mech.* **562**, 383–403.

Weller, T. & Oberlack, M. 2006 DNS of a turbulent channel flow with streamwise rotation – study of the reverse effect of the cross flow. *Proc. Appl. Math. Mech.* **6**, 553–554.

Wu, H. & Kasagi, N. 2004 Effects of arbitrary directional system rotation on turbulent channel flow. *Phys. Fluids* **16**, 979–990.

Yang, Z. & Wang, B.-C. 2018 Capturing Taylor–Görtler vortices in a streamwise-rotating channel at very high rotation numbers. *J. Fluid Mech.* **838**, 658–689.